RSC Advances

PAPER

View Article Online
View Journal | View Issue

Cite this: *RSC Adv.*, 2025, **15**, 38435

Eco-friendly adsorption of a cationic dye using a chemically modified industrial by-product: process optimization and modeling

Soumia Bakhta, *[a] Zahra Sadaoui,[a] Noreddine Boudechiche,[ab] Haroun Hafsa,[a] Karima Sellami[a] and Julien Vieillard[c]

Received 28th July 2025
Accepted 22nd September 2025

DOI: 10.1039/d5ra05466d

rsc.li/rsc-advances

The increasing environmental threat posed by dye-contaminated wastewater, particularly from textile industries, calls for the development of effective and economically viable treatment solutions. Adsorption has emerged as a promising method due to its straightforward application, enhanced efficiency, and economic feasibility. In this study, an industrial by-product from sweet almond oil extraction (sweet almond, SA) was chemically modified with hydrogen peroxide (H_2O_2) to produce an innovative adsorbent material, noted SA-OH, for the removal of Basic Blue 41 (BB41) dye from aqueous solutions. The SA and SA-OH materials were characterized using scanning electron microscopy/energy-dispersive spectroscopy (SEM/EDS), Fourier transform infrared spectroscopy (FTIR), and Brunauer–Emmett–Teller (BET) to investigate their morphological and surface properties. The operational parameters affecting BB41 removal, including solution pH, adsorbent dosage, and initial dye concentration, were optimized using central composite design (CCD) within the framework of the response surface methodology (RSM). Isotherm and kinetic models were applied to describe the biosorption behavior. The results indicated a substantial improvement in the adsorption capacity of SA-OH compared to untreated SA, demonstrating the potential of SA-OH as an effective, cost-efficient, and environmentally sustainable adsorbent for industrial wastewater treatment. To the best of our knowledge, this is the first study reporting the use of hydrogen peroxide-modified sweet almond waste for BB41 dye removal.

1 Introduction

Environmental pollution caused by dye-contaminated wastewater, resulting from rapid industrialization and urbanization, is a global issue.[1] Dyes are widely used in industries such as textiles, printing, plastics, and cosmetics to color products, leading to the generation of large amounts of colored wastewater.[2] Dyes are primarily categorized into anionic, cationic, and non-ionic types. Among all the dyes used in various industries, the textile industry ranks first in terms of dye consumption for fiber coloration.[3] Dyes are chemical substances that bind to fabrics or surface materials to color them.[4]

Treating wastewater from textile and manufacturing industries is a major challenge for environmental managers, as the dyes used are water-soluble and produce highly colored wastewater, often with acidic properties, which pose a potential hazard to the environment.[5] Given the environmental and health concerns related to wastewater effluents, a variety of conventional treatment technologies for dye removal have been thoroughly explored. These include adsorption, coagulation, advanced oxidation, membrane separation, foam flotation, precipitation, ozonation, ion exchange, filtration, solvent extraction, electrolysis, chemical oxidation, and liquid–liquid extraction, which are used for the removal of pollutants from wastewater.[6]

Among these methods, adsorption is considered one of the most effective techniques in separation technology, particularly in wastewater treatment, owing to its significant advantages, such as straightforward design, operational simplicity, and superior separation efficiency relative to other methods.[7] Adsorption is a key unit operation in chemical engineering processes used to separate pollutants from industrial wastewater.[8]

In the quest for affordable and readily available low-cost adsorbents for dye removal from wastewater, a variety of waste-derived materials have been used.[9] These include coconut shells, rice husks, petroleum by-products, tannin-rich materials, sawdust, fertilizer waste, fly ash, by-products from the

---

[a] *Laboratory of Reaction Engineering, Faculty of Mechanical and Processes Engineering, University of Sciences and Technology Houari-Boumediene, BP No. 32, El alia, Bab Ezzouar, 16111 Algiers, Algeria. E-mail: soumia.bakhta64@gmail.com*

[b] *Department of Process Engineering, Faculty of Sciences and Technology, Djilali Bounaama University of Khemis-Miliana, Theniat El-Had Road, Khemis-Miliana, Ain-Defla, Algeria*

[c] *Univ Rouen Normandie, INSA Rouen Normandie, Univ Caen Normandie, ENSICAEN, CNRS, Institut CARMeN UMR 6064, 27000 Evreux, France*

sugar industry, blast furnace slag, chitosan, seafood processing waste, seaweed and algae, peat moss, scrap tires, fruit waste, and others.[10] The wastes that come from different farming and forestry operations are called agricultural wastes.[11] Using farm waste as adsorbents for wastewater treatment is low-cost and the adsorbents are readily available, have a short recovery cycle, are chemically stable, and do not need much processing, in addition to being environmentally benign and sustainable.[12] Agricultural waste and by-products can be converted into efficient adsorbents because they have holes and a relevant surface area, which are important for the design of effective adsorbents for water treatment.[13–16] Recently, the high-value utilization of agricultural wastes has attracted increasing attention, with several studies reporting the conversion of biomass-derived precursors into efficient functional materials for water remediation. For instance, catalysts or bioflocculants prepared from agricultural residues, such as Fe–Ni supported biochar[17] or bioflocculants produced using potato starch wastewater as a fermentation substrate,[18] have shown remarkable efficiency in pollutant removal, highlighting the growing interest in agricultural waste valorization. Similarly, a lot of research has been done on developing ways in which industrial waste and by-products can be used to clean up water and wastewater.[14,15] This type of adsorbent is economically viable because the by-products are easily accessible and require minimal processing.[19] Industrial by-products such as sludge, fly ash, lignin, blast furnace slag, and red mud have been utilized as effective alternative adsorbents to commercial options for removing contaminants from wastewater.[15,16] Kraft lignin is an industrial form of lignin derived from Kraft pulp, accounting for approximately 85% of the global lignin production.[20] Recent reports have highlighted Kraft lignin as a valuable material for the decontamination of water and wastewater.[16] Sludge is a semi-solid or slurry by-product generated from various industrial processes, including water treatment, wastewater treatment, and on-site sanitation systems,[21] and it is frequently used as an adsorbent to remove pollutants from aqueous solutions.[22]

Adsorption is a surface technique. The effectiveness of an adsorbent is determined by its surface chemistry.[23] Thus, enhancing the quality of the adsorbent's surface is crucial to improve the selectivity and the adsorption capacity.[7] Surface modification can be achieved through various methods, including both physical and chemical processes.[24,25] Chemical surface modification is preferred for adsorbents as it directly affects the surface chemistry of the material. This method enables the transformation of affordable materials from various precursors into valuable products with significantly improved adsorptive capacities.[23] Chemical methods involve the application of acids, alkalis, or salts to modify the surface functional groups, while physical processes focus on improving properties such as density, solubility, and overall structure.[23] Chemical modification can be performed utilizing a range of reagents, including oxidizing agents such as potassium permanganate and hydrogen peroxide, and neutral agents such as $ZnCl_2$ and NaCl, and through metal impregnation with ferric chloride, cerium, zirconium, hydroxides, carbonates, chromates, or nitrates, as well as organic agents such as ethanol.[26] Oxidizing agents increase the presence of oxygen-containing functional groups on the adsorbents.[27]

The response surface methodology (RSM) integrates statistical and mathematical techniques to design, enhance, and optimize processes.[28] This approach aids in assessing the significance of different process parameters, especially in contexts characterized by intricate interactions.[29] RSM has found applications across multiple disciplines, such as chemistry, physics, biology, and water treatment. The use of dye biosorption *via* response surface methodology enables the fitting of mathematical models to experimental data, thereby reducing the number of experiments needed and facilitating the identification of optimal parameters.[30] This method aims to improve the efficiency of water treatment by optimizing time and cost expenditures.[31] RSM is an effective tool for predicting engineering processes and is widely applied in various design methodologies, such as Box–Behnken, Doehlert, central composite design (CCD), and central composite rotatable designs (CCRD), to optimize and model complex systems.[32] The CCRD method combines factorial points from a full factorial (2^k), axial points ($2k$), and center points (cp). The total number of experiments is calculated as $N = 2^k + 2k + \text{cp}$, where k represents the number of factors, and cp is the number of central point replicates.[33] Central composite design (CCD) is an RSM approach that recommends a series of experiments aimed at achieving optimization using the minimal number of tests.[34] However, in certain cases, the first-order and quadratic models developed using RSM may not accurately fit the experimental data.[35] Although cubic regression functions are rarely applied to experimental data, they become crucial when the response variable is sensitive to changes in the parameters. In such cases, the interaction between the parameters plays a vital role, and a third-order model offers a more comprehensive understanding of the process's nature.[36] Podstawczyk *et al.* examined the impact of various operating parameters on Cu^{2+} removal within a concentration range of 20–200 mg L^{-1}, biosorbent doses of 1–10 g L^{-1}, and pH levels between 2 and 5.[37] They modeled these parameters by comparing three experimental designs: CCD, Box–Behnken design (BBD), and full factorial design (FFD). The second-order polynomial equation, extended with additional cubic effects, was utilized as the objective function. The authors demonstrated that CCD emerged as the most effective design among the experiments for modeling the impact of process conditions, based on the correlation coefficient ($R^2 = 0.99$) and ANOVA (Fisher value of 276 with a *p*-value lower than 0). The resulting model was then used to determine the optimal conditions that maximize biosorption yield, as indicated by metal removal. The objective of our study was to valorize an industrial by-product generated during the extraction of vegetable oil from sweet almond seeds (SA), which was further modified *via* surface treatment with hydrogen peroxide. To the best of our knowledge, the use of this industrial waste as a precursor for BB41 dye adsorption has not been reported. The adsorption capacity of the newly developed material, termed SA-OH, was tested for BB41 removal from aqueous solutions. Given its potential, SA-OH offers an economically viable alternative to high-cost biosorbents, thereby providing a promising solution for industrial applications. The material was characterized using scanning electron microscopy coupled with energy-dispersive spectroscopy (SEM/EDS), Fourier transform infrared spectroscopy (FTIR), and Brunauer–Emmett–Teller (BET) surface area analysis. Furthermore, CCD was employed to optimize operational parameters affecting BB41 removal, including solution pH, biosorbent dose, and initial BB41 concentration, to achieve optimal performance. Furthermore, relevant biosorption isotherm and kinetic models were applied to describe the BB41 biosorption process.

2 Materials and methods

2.1 Chemicals

All chemicals used in this study were of analytical grade and were used without further purification. Hydrogen peroxide (H_2O_2, 30% w/v) (used for the chemical surface modification of the sweet almond waste) and calcium chloride were supplied by VWR Chemicals. The cationic dye Basic Blue 41 (BB41) was from Sigma-Aldrich. Stock solutions of BB41 (1000 mg L^{-1}) were prepared by dissolving an appropriate amount of the dye in distilled water and subsequently diluted to the required concentrations for adsorption experiments. The pH of the solutions was adjusted using hydrochloric acid (HCl, 0.1 M) or sodium hydroxide (NaOH, 0.1 M), both sourced from Sigma-Aldrich.

2.2 Biosorbent preparation

The sweet almond (SA) selected as the raw material for biosorbent preparation was obtained as an agro-industrial by-product from an Algerian company specializing in aromatic and medicinal plants and products (AMPP). This company operates in the production and commercialization of herbal products, condiment plants, essential oils, vegetable oils, oily macerates, hydrosols, and various plant-based agri-food goods on a global scale. The raw biomass was pretreated to ensure repeatability. First, the material was thoroughly cleansed with distilled water to remove any surface contaminants. It was then oven-dried at 50 °C overnight to remove any remaining moisture. The dried biomass was subsequently ground using a mechanical grinder and sieved through a standard mesh to obtain a uniform particle size fraction of 0.2–0.3 mm. Finally, the pretreated biosorbent was stored in a desiccator until further use.

2.3 Preparation of the modified adsorbent (SA-OH)

To introduce hydroxyl (OH) groups onto the biosorbent surface, a hydroxylation treatment was performed. The biosorbent sample was dispersed in a solution containing hydrogen peroxide (30% w/v), sodium hydroxide (2 M), and ultrapure water (1 : 1 : 5 v/v/v, respectively), and stirred continuously for 4 hours at room temperature (25 °C). The treated biomass was then filtered, thoroughly rinsed with deionized water, and oven-dried overnight at 80 °C. The resulting hydroxylated material is hereafter designated as SA-OH. The preparation steps are shown schematically in Fig. 1.

2.4 Characterization of the adsorbent

The specific surface area and pore size distribution of SA and SA-OH were determined from the nitrogen adsorption isotherms at liquid-nitrogen temperature (77.5 K) using a Micromeritics ASAP 2020. The pore size distribution was calculated from the adsorption isotherms based on density functional theory (DFT). The functional groups present in the SA and SA-OH were determined using Fourier-transformed infrared spectroscopy (FTIR). FTIR measurements were carried out on a Bruker Vertex 60 spectrometer at room temperature in the wavenumber range of 650–4000 cm^{-1}. Field-emission scanning electron microscopy (FESEM, Zeiss Ultra Plus) coupled with energy-dispersive X-ray spectroscopy (EDS) was employed to investigate the morphology characteristics of the raw precursor and the SA-OH. The samples were coated with carbon to ensure sufficient conductivity. In addition, the elemental chemical composition of the samples was obtained using an EDS analyzer. Zeta potential was determined using a Malvern Zetasizer Nano ZS, and the samples were prepared by dispersing 0.1 g of adsorbents in 10 mL of distilled water.

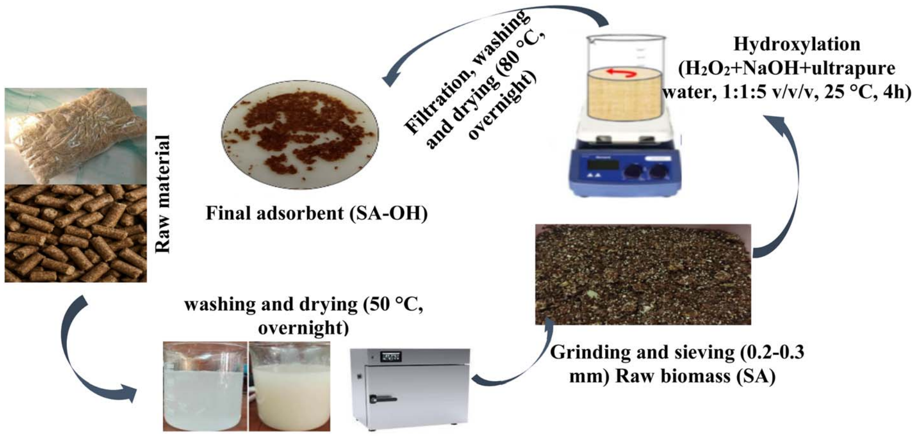

Fig. 1 Schematic of the preparation of SA-OH material.

Table 1 Molecular properties of Basic Blue 41

Molecular formula	$C_{20}H_{26}N_4O_6S_2$
Molecular weight (g mol^{-1})	482.6
Color index	11 105
Synonyms	C.I. Basic Blue 41, 2-[*N*-ethyl-4-[(6-methoxy-3-methyl-1,3-benzothiazol-3-ium-2-yl)-diazenyl]anilino]ethanol methyl sulfate
Chemical structure of BB41	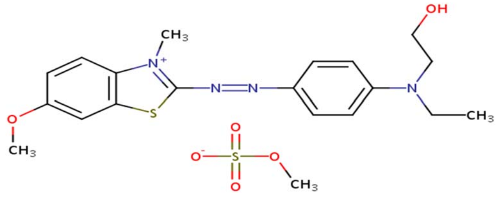

Table 2 Experimental factors and their ranges and standard deviations

Parameters	Units	Factor code	Coded levels and actual values				
			Low axial ($-\alpha = -1.68$)	Low factorial −1	Central (0)	High factorial +1	High axial ($+\alpha = +1.68$)
Solution pH	—	X_1	1.997	3.01	4.495	5.98	6.992
Biosorbent dose	g L^{-1}	X_2	0.989	1.6	2.495	3.39	4
Initial BB41 concentration	mg L^{-1}	X_3	49.59	201.78	424.995	648.21	800.39
$\alpha = (2^k)^{1/4}$	—	—	—	—	—	—	—

2.5 Preparation of aqueous BB41 solution

BB41 was supplied by the TEXALG textile unit located in Bab El Zouar (Algiers, Algeria). A stock solution was prepared by dissolving 1 g of BB41 in 1 L of distilled water. Working solutions with concentrations ranging from 50 to 800 mg L^{-1} were obtained by serial dilution of the stock solution. BB41 is an anionic dye, and its maximum absorption wavelength (λ_{max}) is 610 nm; additional physicochemical properties are reported in Table 1.

2.6 Batch adsorption experiments

Batch adsorption experiments were conducted to assess the performance of SA-OH for BB41 removal. The experiments were performed in 50 mL Erlenmeyer flasks containing 25 mL of BB41 solution at predetermined initial concentrations. The flasks were agitated in an orbital shaker at a constant speed of 250 rpm under room temperature conditions. After a defined contact time, the suspensions were filtered, and the residual concentration of BB41 in the filtrate was quantified spectrophotometrically at 610 nm using an Optizen 2120 UV-Vis spectrophotometer.

The amount of BB41 adsorbed at equilibrium (q_e, mg g^{-1}) and the removal efficiency (%) were calculated according to the following equations:[38,39]

$$q_t = \frac{(c_0 - c_t)}{m} \times V \tag{1}$$

$$\text{Removal}(\%) = \frac{(c_0 - c_t)}{c_0} \times 100 \tag{2}$$

where C_0 represents the initial BB41 concentration (mg L^{-1}), C_t denotes the BB41 concentration at time t (mg L^{-1}), m is the mass of the biosorbent (g), and V is the solution volume (L).

2.7 Response surface modeling and experimental design

Response surface methodology (RSM) with a central composite design (CCD) was applied to optimize BB41 dye removal. Three factors were studied: solution pH (X_1), biosorbent dose (X_2), and initial BB41 concentration (X_3). Each factor was evaluated at five levels ($-\alpha$, -1, 0, +1, $+\alpha$), generating a total of 16 runs (8 factorial, 6 axial, and 2 center points). The design was generated using JMP 11.0 (SAS Institute).

The coded values (x_j) for the process variables were derived from eqn (3).[40]

$$x_j = \frac{Z_j - Z_j^{\,0}}{\Delta Z_j} \tag{3}$$

With:

$$Z_j^{\,0} = \frac{Z_{j\max} + Z_{j\min}}{2} \tag{4}$$

$$\Delta Z_j = \frac{Z_{j\max} - Z_{j\min}}{2\alpha} \tag{5}$$

where x_j represents the coded value of variable j, Z_j denotes the actual value, $Z_j^{\,0}$ is the value of Z_j at the center point of the

Table 3 Central composite rotatable design matrix with experimental and predicted values[a]

Runs	pH	Biosorbent dose	Initial BB41 concentration	Removal experimental (%) Y_1 (SA)	Removal predicted (%) Y_1 (SA)	Removal experimental (%) Y_2 (SA-OH)	Removal predicted (%) Y_2 (SA-OH)
1	4.495	2.95	49.936	63.3	64.088	90.8	91.79
2	3.1	1	201.8	42.3	42.88	38.5	37.81
3	5.8	1	201.8	69.9	69.614	95.3	94.97
4	3.1	3.9	201.8	60.7	57.77	55.6	52.89
5	5.8	3.9	201.8	64.3	66.90	80.3	83.50
6	4.95	0.89	424.95	35.8	36.58	28.5	31.68
7	1.97	2.95	424.95	33.2	37.09	23.6	28.02
8	4.95	2.95	424.95	69.9	69.45	70.1	69.14
9	4.95	2.95	424.95	69.7	69.455	69.1	69.14
10	6.92	2.95	424.95	66.5	64.10	75.8	73.16
11	4.95	4	424.95	70	71.71	62.5	62.109
12	3.1	1	648.1	16.1	12.29	21.8	17.47
13	5.8	1	648.1	34.3	36.01	38.4	40.98
14	3.1	3.9	648.1	57.3	56.380	65.9	65.10
15	5.8	3.9	648.1	64.3	62.50	61.5	61.06
16	4.95	2.95	800.96	34	35.71	55.9	57.698

[a] Y_1: represents the adsorption efficiency of the raw adsorbent. Y_2: represents the adsorption efficiency of the adsorbent after treatment.

experimental domain, and ΔZ_j is the step size. Here, $Z_{j\max}$ and $Z_{j\min}$ represent the maximum and the minimum levels of factor j, respectively.

The correlation of the independent variables and the response was estimated by a second-order polynomial (eqn (6)), using the least-squares method, as shown below:[41]

$$Y = a_0 + \sum_{i=1}^{n} a_i x_i + \sum_{i=1}^{n} a_{ii} {x_i}^2 + \sum_{i=1}^{n-1} \sum_{j=i+1}^{n} a_{ij} x_i x_j \tag{6}$$

In this equation, Y represents the predicted response, while a_0, a_i, $a_{ii,}$ and a_{ij} denote the constant, linear, quadratic, and interaction coefficients, respectively, expressed in terms of the coded variables x_i and x_j. Table 2 presents the coded and real values of the independent variables.

The adequacy of the model was evaluated using analysis of variance (ANOVA) and lack-of-fit testing, while model validation was performed by comparing predicted and experimental responses (Table 3).

3 Results and discussion

3.1 FTIR analysis

The functional groups present on the surface of the different adsorbents, SA, SA-OH, and SA-OH after adsorption, were identified by FTIR analysis. As shown in Fig. 2, absorption bands at 3400, 2926, 2852, 1735,1662 cm^{-1}, 1240 cm^{-1}, 1158 cm^{-1} and 1030 cm^{-1}, which correspond to O–H,[29] ν_as(CH$_2$)[37] and ν_s(CH$_2$) of aliphatic groups,[42] C=O of esters/acids (hemicellulose/lignin conjugates),[32] aromatic C=C of lignin,[43] C–O–C/aryl–O linkages in lignin and polysaccharides,[44] ν_as(C–O–C) of β-glycosidic linkages in cellulose and C–O stretching in polysaccharides,[33,34] were observed in all three spectra, with variations in intensity. These bands confirm the lignocellulosic nature of the material, which is composed of cellulose, hemicellulose, and lignin. After hydrogen peroxide treatment (SA–OH), the O–H band at 3400 cm^{-1} intensified, indicating the formation of new hydroxyl groups.[30] The peaks at 2926 and 2852 cm^{-1} became more prominent due to increased exposure of aliphatic CH$_2$ groups after partial delignification.[38] A new band appeared around 1635 cm^{-1}, typically assigned to the bending vibration of adsorbed/bound water (δ(H–O–H)), consistent with the increased hydrophilicity induced by H_2O_2 oxidation.[45] The peak at 1662 cm^{-1} was significantly weakened after H_2O_2 treatment, which can be attributed to oxidative breakdown of lignin structures and reduced aromatic conjugation.[46] Similarly, the 1240 cm^{-1} peak, attributed to C–O–C linkages in polysaccharides (cellulose and hemicellulose), decreased in intensity, indicating the oxidation of ether bonds and aryl–O linkages induced by H_2O_2 treatment.[47] Conversely, the 1158 cm^{-1} peak, assigned to asymmetric C–O–C stretching of β-glycosidic linkages in cellulose, increased due to cellulose

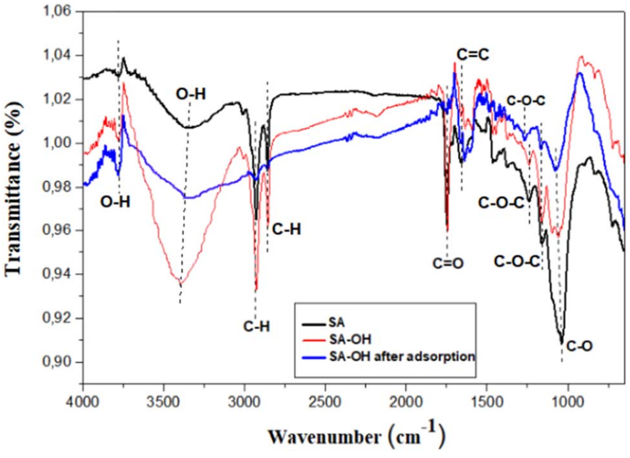

Fig. 2 FTIR spectra of unmodified SA and modified SA before and after adsorption.

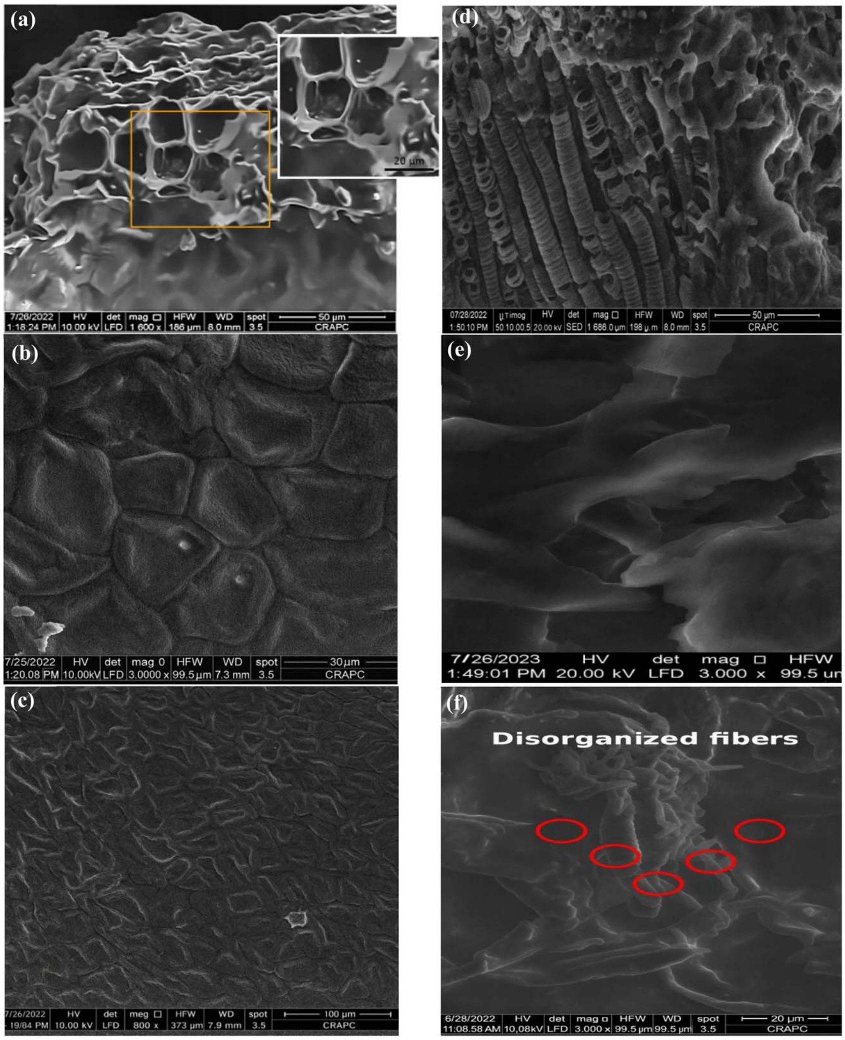

Fig. 3 FESEM micrographs illustrating the morphological evolution of sweet almond (SA) biomass before treatment (a–c) and after chemical treatment (d–f).

enrichment after partial delignification and reduced band overlap upon oxidation.[48] Likewise, the 1030 cm^{-1} band decreased, likely due to the formation of hydroxyl groups and rearranged hydrogen bonding, which altered the C–O stretching.[35] These results confirm the structural modifications induced by H_2O_2 oxidation. After BB41 adsorption, the intensity of the O–H band declined due to interactions between the dye and hydroxyl groups.[31] The peaks at 2926, 2852, 1735, 1240, and 1030 cm^{-1} were further reduced, confirming chemical interactions between the BB41 molecules and the functional groups on the SA–OH surface.[36] Additionally, the 1158 cm^{-1} peak (ν_as(C–O–C) of β-glycosidic linkages in cellulose) decreased in intensity, which we attribute to dye–polysaccharide complexation and hydrogen bonding that reduce the dipole-moment change of this vibration.[49] The 1662 cm^{-1} peak increased again, likely due to overlapping contributions from the aromatic rings of BB41, suggesting π–π stacking interactions between dye molecules and the aromatic domains of the modified adsorbent.[50] Additionally, the 1635 cm^{-1} band increased after BB41 adsorption, consistent with stronger bound-water bending (δ(H–O–H)[45] and partial overlap with dye aromatic/N–H modes. Notably, the 1240 cm^{-1} peak not only diminished further but also shifted slightly to lower wavenumbers, reflecting a weakening of the C–O–C peak environment due to strong interactions with the dye molecules.[51] Such changes in surface vibrational modes and adsorption affinities align with previous reports emphasizing the synergistic role of ionic and organic species in modifying surface reactivity, as demonstrated by Fu *et al.*[52]

3.2 FESEM/EDS analysis

Field-emission scanning electron microscopy (FESEM) coupled with energy-dispersive X-ray spectroscopy (EDS) was employed to investigate the morphology of raw (SA) and treated sweet almond (SA-OH), together with their elemental chemical composition. The SEM micrographs of the materials are presented in Fig. 3. The SEM analysis revealed significant differences between untreated biomass and biomass treated with

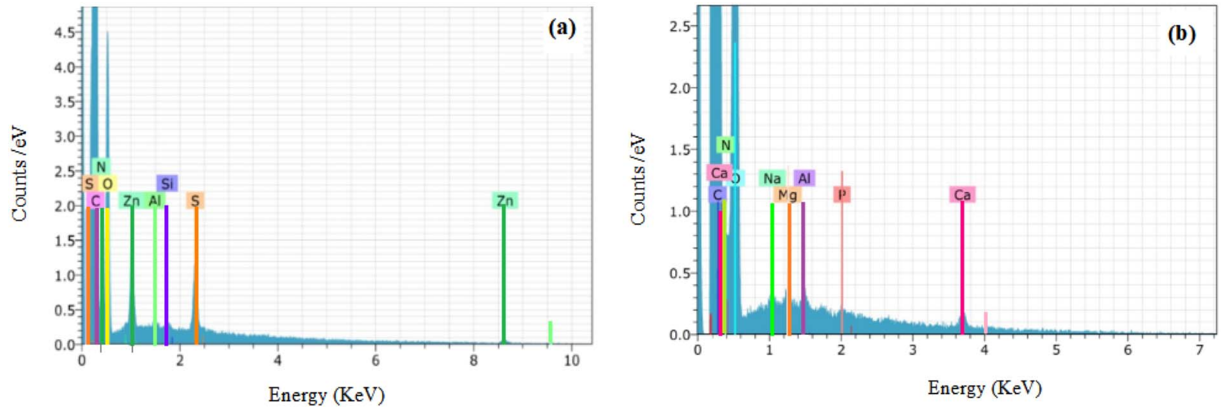

Fig. 4 Energy-dispersive X-ray fluorescence spectra of SA before (a) and after (b) treatment.

hydrogen peroxide and sodium hydroxide. Before treatment, the biomass exhibited a complex, thick fibrous structure, with low apparent porosity. Pores were often blocked by organic materials such as lignin and hemicellulose, limiting the active surface area. The texture was primarily uniform, with some roughness and a well-organized fiber structure.[53] The structure was more porous, with larger and deeper cavities, following treatment, suggesting the partial dissolution of lignocellulosic components such as hemicellulose and lignin. The material was characterized by fiber fragmentation and fissuring, resulting in a rougher and more irregular surface. The delignification and structural degradation induced by NaOH/H_2O_2 treatment were consistent with the progressive disorganization of the plant cell walls, as indicated by the morphological changes shown in Fig. 3f.[54] The oxidative delignification induced by hydrogen peroxide and the saponification by NaOH, which facilitated the disintegration of structural polymers and promoted pore formation, were confirmed by the erosion of superficial structures.[55–59] These modifications enhanced the accessibility of internal surfaces and established a more heterogeneous texture. This treatment increased the specific surface area by removing obstructive components and improving access to active sites, thereby enhancing the material's reactivity and suitability for applications in adsorption, catalysis, and bio-based material development.

Table 4 Elemental composition of sweet almond biomass (SA) before and after chemical treatment (SA-OH)

	Untreated biomass (SA)		Treated biomass (SA-OH)	
Element	(wt%)	(A%)	(wt%)	(A%)
C	58.38	65.23	48.38	55
O	27.45	23.02	41.23	35.19
N	11.35	10.87	9.80	9.55
S	1.14	0.48	—	—
Zn	1.50	0.31	—	—
Si	0.09	0.04	—	—
Al	0.1	0.05	0.08	0.04
Na	—	—	0.05	0.03
Mg	—	—	0.06	0.04
Ca	—	—	0.36	0.12
P	—	—	0.05	0.02

EDS analysis (Fig. 4 and Table 4) of the raw biomass revealed a high carbon content (58.38 wt%) and oxygen (27.45 wt%), which is characteristic of an organic matrix rich in carbon-based compounds such as cellulose, hemicellulose, and lignin. Nitrogen (11.3 wt%) was also detected, indicating the presence of proteins or other nitrogenous compounds. Additionally, trace amounts of mineral elements such as sulfur (1.1 wt%), zinc (1.5 wt%), silicon (0.1 wt%), and aluminum (0.1 wt%) were detected, likely originating from natural mineral residues or environmental impurities. After treatment with hydrogen peroxide (H_2O_2) and sodium hydroxide (NaOH), significant chemical changes were observed. The oxygen content increased to 41.2 wt%, indicating enhanced oxidation and the formation of oxygen-containing functional groups (*e.g.*, hydroxyl and carboxyl),[58–60] which improve the material's adsorption potential. At the same time, the carbon content decreased to 48.38 wt%, suggesting partial degradation of organic compounds as a result of alkaline treatment. Furthermore, certain mineral elements, such as sulfur and zinc, were no longer detected after treatment, while new traces of sodium (0.05 wt%), magnesium (0.06 wt%), calcium (0.36 wt%), and phosphorus (0.05 wt%) appeared, originating from the sodium hydroxide used or other environmental sources. These results show that the chemical oxidation and chemical modification of the biomass, while removing certain mineral impurities, could enhance its properties for specific applications such as adsorption.

3.3 Textural properties

The characterization results of the adsorbents SA and SA-OH, with their surface areas, pore sizes, pore volumes, and pore size distributions, are summarized in Table 5. The BET results indicate a major structural transformation. The raw biomass had a low specific surface area (2.62 $m^2\ g^{-1}$) and total pore volume (0.000101 $cm^3\ g^{-1}$), indicating a dense and weakly porous structure.[38] After treatment, the biomass was significantly activated, with a specific surface area of 885.51 $m^2\ g^{-1}$,

Table 5 Specific surface area (BET), pore volume, pore size, and pore distribution of SA and SA-OH

Adsorbent	S_{BET} ($\mathrm{m^2\ g^{-1}}$)	Total pore volume (V_T) ($\mathrm{cm^3\ g^{-1}}$)	Mean pore diameter (nm)	Pore distribution (%) Micropores	Mesopores	Macropores	Microporous surface ($\mathrm{m^2\ g^{-1}}$)
SA	2.62	0.000101	28.95	8.14	65	26.54	—
SA-OH	885.61	0.3898	9.44	22	76	2	204.73

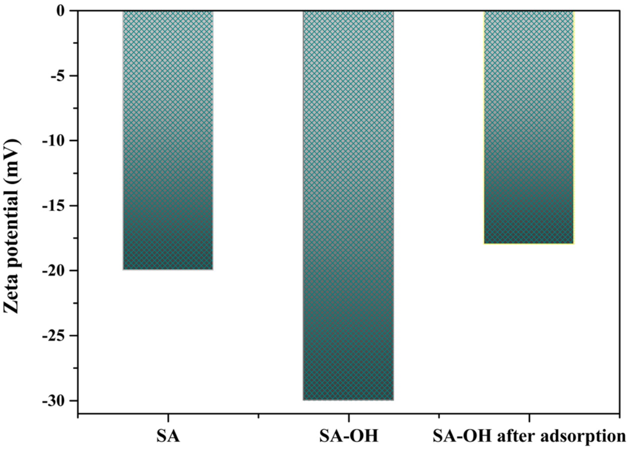

Fig. 5 Zeta potential of SA, SA-OH, and SA-OH after BB41 adsorption.

reflecting an opening of the porous structure. The total pore volume rose to 0.3898 $\mathrm{cm^3\ g^{-1}}$, reflecting a significant increase in the porosity.[58,59] Transformation results from the combined effects of H_2O_2, a strong oxidant that removes impurities and introduces oxygenated functional groups, and NaOH, which activates the biomass by dissolving lignin and hemicellulose, thereby facilitating pore expansion.[60] BJH analysis marked a change in the porosity of the biomass following chemical treatment with H_2O_2 + NaOH. Before treatment, the raw biomass was predominantly mesoporous (65.32%) but with a high proportion of macropores (26.54%), which limited its adsorption capacity. With only 8.14% micropores and a small specific surface area, its interaction with gases and liquids was negligible. Following treatment, the biomass underwent a major structural reorganization, with a noticeable increase in micropores (22%) and mesopores (76%), while the proportion of macropores decreased to 2%, indicating a significant expansion and opening of the pore network. The mean pore diameter, as determined by BJH analysis, decreased from 28.95 nm for SA to 9.44 nm for SA-OH; both values fall within the mesoporous range defined by the IUPAC classification (2–50 nm). Hydrogen peroxide oxidized contaminants and oxygenated functional groups, whereas sodium hydroxide degraded lignin and hemicellulose to form a porous structure. The specific surface area rose from 2.62 $\mathrm{m^2\ g^{-1}}$ to 885.51 $\mathrm{m^2\ g^{-1}}$, while the microporous surface reached 204.73 $\mathrm{m^2\ g^{-1}}$. This enhances the material's adsorption properties. The findings confirmed the effective conversion of a dense and weakly porous biomass into a well-structured material suitable for adsorption applications.[61]

3.4 Zeta potential

The zeta potential is the electrostatic potential at the interface between the dispersion medium and the fluid layer surrounding a dispersed particle. It is a useful metric for assessing the surface charge and acidity of adsorbent surfaces, as well as providing information about their stability and interaction potential in various environments. The zeta potential test indicated a marked change in the surface charge of the biomass after chemical treatment and cationic dye adsorption (Fig. 5). The raw biomass (SA) showed a zeta potential of −20 mV, indicating a distinctly negative charge. The raw biomass showed limited adsorption capacity for cationic dyes due to the presence of hydroxyl (–OH) and carboxyl ($\mathrm{COO^-}$) functional groups. Treatment with H_2O_2 + NaOH shifted the zeta potential to −30 mV, indicating a higher negative charge density. This change was attributed to oxidation by H_2O_2, which introduces carboxyl ($\mathrm{COO^-}$), carbonyl (C═O), and phenolic (OH) groups, and to the action of NaOH, which further activates these functional sites, thereby strengthening electrostatic interactions with cations.[62] After dye adsorption, the zeta potential rose to −18 mV, showing that negative charges are partially neutralized by dye molecules attached to the adsorbent surface. These findings show that chemical treatment changes the surface functionalization, surface negative charge density, and adsorption capacity, making the biomass more effective for capturing cationic contaminants.[61]

3.5 BB41 adsorption efficiency of the different adsorbents

A selectivity study was conducted to identify the most effective adsorbent for the removal of BB41 dye, based on adsorption

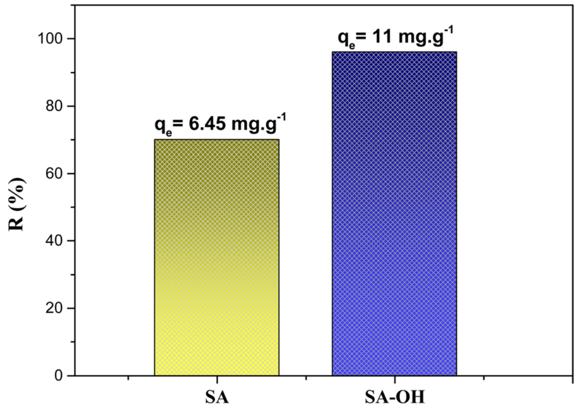

Fig. 6 Adsorption efficiency of BB41 dye onto SA and SA-OH adsorbents.

Table 6 ANOVA and lack of fit test for the response surface quadratic model

	Degree of freedom		Sum of squares		Mean square		F value		p value	
Source	SA	SA-OH	SA	SA-OH	SA	SA-OH	SA	SA-OH	SA	SA-OH
Regression	9	9	4654.114	7721.05	517.125	857.9	42.82	61.2	0.001	0.001
Residues	6	6	72.451	84.89	12.075	14.015				
Total	15	15	4726.565	7805.995						
Lack of fit	5	5	77.897	80 615	15.579	16.123	25.966	32.246	0.185	0.139
Pure error	1	1	0.6	0.5	0.6	0.5				
Total	6	6	78.497	81 115						

performance. Adsorption experiments were conducted using the adsorbents SA and SA-OH under the following conditions: adsorbent dose = 3 g L^{-1}, initial BB41 concentration = 20 mg L^{-1}, temperature = 23 °C, contact time = 3 h, and pH 5.95. The corresponding results are presented in Fig. 6. Of the two materials tested, SA-OH was found to exhibit a significantly higher adsorption efficiency, reaching approximately 95% (q_e = 11 mg g^{-1}), in contrast to the raw SA, which was observed to show considerably lower performance (65%, q_e = 6.45 mg g^{-1}). This enhanced adsorption capacity is attributed to the chemical treatment of SA, which increased the number of active sites and improved the surface characteristics of the material. Based on these findings, both SA and SA-OH were considered for further optimization studies to evaluate their adsorption potential in greater detail.

3.6 Experimental design

3.6.1 Analysis of variance. Quadratic mathematical models are often insufficient for accurately describing experimental data. A more reliable model may be required to improve the fit assessment using ANOVA and to compare sources of variation through the Fisher distribution (Fisher test). This statistical test is based on the ratio between the error sum of squares and the regression sum of squares. Accordingly, the significance of the regression is assessed by the ratio of the regression mean square to the residual mean square, which reflects the difference between observed and predicted values.[63,64] ANOVA results for the quadratic equations (Table 6) indicate that the Fisher values for all regressions are high. A high Fisher value suggests that the quadratic model effectively explains the variation in BB41 removal. The associated p-value is used to determine whether the Fisher value is sufficiently large to demonstrate statistical significance. A p-value below 5% (*i.e.*, $\alpha = 0.05$, representing a 5% error or 95% confidence) indicates that the model is statistically significant.[65] The computed Fisher values for the regression models are 42.82 for raw biomass and 61.22 for treated biomass, both exceeding the critical Fisher value ($F_{9,6} = 3.37$). Additionally, the extremely low probability values ($p < 0.001$) confirm that the regression models describing BB41 removal are statistically significant at a 95% confidence level. Moreover, the lack-of-fit test was found to be non-significant for both models (p = 0.189 for SA and p = 0.139 for SA-OH), as presented in Table 6. This finding indicates that the deviations can be attributed to pure experimental error rather than model inadequacy, confirming that the quadratic models adequately describe BB41 removal for both adsorbents.

3.6.2 Prediction quality (R^2, adjusted R^2). Eqn (2) was employed to visualize the influence of the experimental parameters on BB41 removal (Fig. 7). The actual values were measured through experiments, whereas the predicted values were calculated using eqn (6). Both the actual and predicted dye removal values are presented in Fig. 6. The R^2 values were 0.98 for SA and 0.99 for SA-OH, with an adjusted R^2 of 0.96 for both

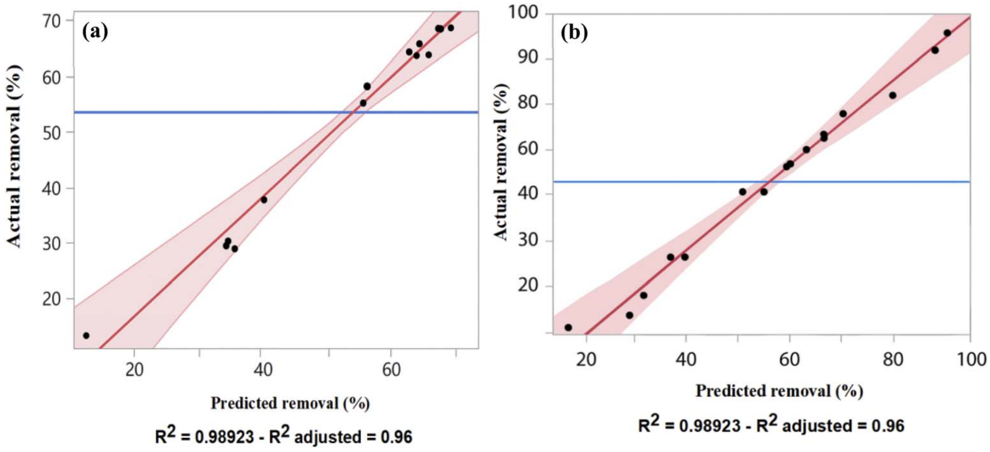

Fig. 7 Actual and predicted values for BB41 removal by (a) SA and (b) SA-OH.

Table 7 Statistical analysis of coefficients from the cubic model[a]

		Estimate parameter		Standard error		Student t-value		p-value	
Coefficient		SA	SA-OH	SA	SA-OH	SA	SA-OH	SA	SA-OH
Constant	a_0	69.96704	69.14449	2.12427	2.39395	31.2	26.0	<0.001*	<0.001*
X_1	a_1	8.157705	13.53104	0.49148	1.13022	9.9	13.8	<0.001*	<0.001*
X_2	a_2	10.09427	9.289364	0.49148	1.13022	12.6	9.1	<0.001*	<0.001*
X_3	a_3	−7.24785	−8.1926	0.49148	1.13022	−8.2	−8.9	<0.001*	<0.001*
$X_1{*}X_2$	a_{12}	−4.9	−6.8875	1.09465	1.23577	−3.6	−5.5	0.075*	0.023*
$X_1{*}X_3$	a_{13}	−0.5	−8.1625	1.09465	1.23577	−0.9	−6.1	0.0793	0.006*
$X_2{*}X_3$	a_{23}	7.55	8.6375	1.09465	1.23577	6.3	6.7	0.006*	0.008*
$X_1{*}X_1$	a_{11}	−6.81809	−6.30787	1.30994	1.29962	−6.9	−5.9	0.007*	0.017*
$X_2{*}X_2$	a_{22}	−5.0881	−8.69749	1.30994	1.29962	−5.1	−6.6	0.015*	0.006*
$X_3{*}X_3$	a_{33}	−7.90441	−1.714096	1.30994	1.29962	−6.6	−1.4	0.005*	0.999

[a] p, probability, * significant critical Student's t-test = 2.45.

adsorbents. These results indicate a strong correlation between the experimental and predicted responses. The results further suggest that the selected quadratic model effectively predicts the response variables for the studied parameters.

3.6.3 Principal interaction effects and Student's *t*-test. To identify the main effects and interactions between factors, regression analysis was conducted. The effect of a factor is defined as the change in response caused by a variation in its level.[66] The regression coefficients, their associated standard errors, Student's t-values, and their effects are presented in Tables 3 and 7. The resulting expression was obtained by inserting the coefficient values from Tables 3 and 6 into eqn (7) and (8), to give the following expressions:

$$Y_1 = 69.967 + 8.157X_1 + 10.094X_2 - 7.247X_3 - 4.9X_1X_2 - 0.5X_1X_3 + 7.55X_2X_3 - 6.818X_1X_1 - 5.088X_2X_2 - 7.904X_3X_3 \tag{7}$$

$$Y_2 = 69.144 + 13.531X_1 + 9.289X_2 - 8.192X_3 - 6.887X_1X_2 - 8.162X_1X_3 + 8.637X_2X_3 - 6.307X_1X_1 - 8.697X_2X_2 - 1.714096X_3X_3 \tag{8}$$

The coefficient sign (±) indicates the direction of the relationship between the associated effect and its corresponding response. A positive sign implies that as the value of one effect increases or decreases, the response follows the same direction. Conversely, a negative sign denotes that the response moves in the opposite direction. The absolute coefficients reflect the strength of the relationship. Table 7 provides a summary of the regression coefficients along with their standard errors, Student's t-values, and corresponding p-values. The p-values and Student's t-values are used to assess the significance of the model coefficients. A higher Student's t-value corresponds to a lower p-value, indicating a highly significant coefficient.[67] According to Table 7, the effects of the three parameters on the adsorption yield of BB41 were found to be significant ($P < 0.001$) for both adsorbents.[63,64] It is followed, to a lesser extent, by second-order interaction effects. Third-order interactions are not reported in the table, as they are not relevant. For the raw biomass (SA), the most influential factor was identified as X_2 (biosorbent dose), followed by X_1 (pH) and X_3 (initial DB41 concentration). However, for the treated biomass (SA-OH), the order of influence changed, with X_1 (pH) exerting the greatest impact, followed by X_2 (biosorbent dose) and X_3 (initial DB41 concentration), because the absolute Student's t-value was lower than the critical Student's t-value, with a probability of $p < 0.001$. The next highly significant effects (|Student's t-value| < critical Student's t-value with $p < 0.08$) included the interactions X_1X_2, X_2X_3, X_1X_1, and X_2X_2 for both adsorbents. Some effects were excluded due to their lack of statistical significance, including X_1X_3 and X_3X_3 for biomass and treated biomass, respectively.

3.6.4 Optimization of independent parameters. RSM, in conjunction with CCD, was applied to optimize factors and visualize response surface characteristics in the experiment *via* three-dimensional (3D) response surface plots. The primary factors and their interactions were effectively identified, facilitating a clear evaluation of the impact of independent variables on the removal percentage.[68] The quadratic polynomial model (eqn (6)) was used to generate the 3D response surface plots for the measured removal percentage. The three-dimensional response surface graphs in Fig. 8 illustrate the impact of two concurrent parameters, with the third parameter maintained at its central level ($X = 0$). The 3D response surface plots revealed clear interactions between the studied variables and BB41 removal efficiency.[69–72] Fig. 8(a and b) show the response surface plot illustrating the interaction between pH and biosorbent dose for biomass and treated biomass, respectively. The elimination of BB41 increased significantly as the pH rose from 3.01 to 6.99, alongside a rise in the biosorbent dosage from 1.8 to 4 mg L^{-1}. At higher pH levels, the biosorbent surface became negatively charged due to the deprotonation of acidic functional groups, such as COO$^-$ and OH$^-$. The presence of anionic groups enhanced the electrostatic attraction of cationic BB41 molecules. Elevating the dosage of the biosorbent improved adsorption by providing more active sites until saturation was reached. Thus, the adsorption process achieved higher efficiency through stronger electrostatic interactions with BB41 molecules.[73,74] Fig. 8(c and d) depict response surface plots for

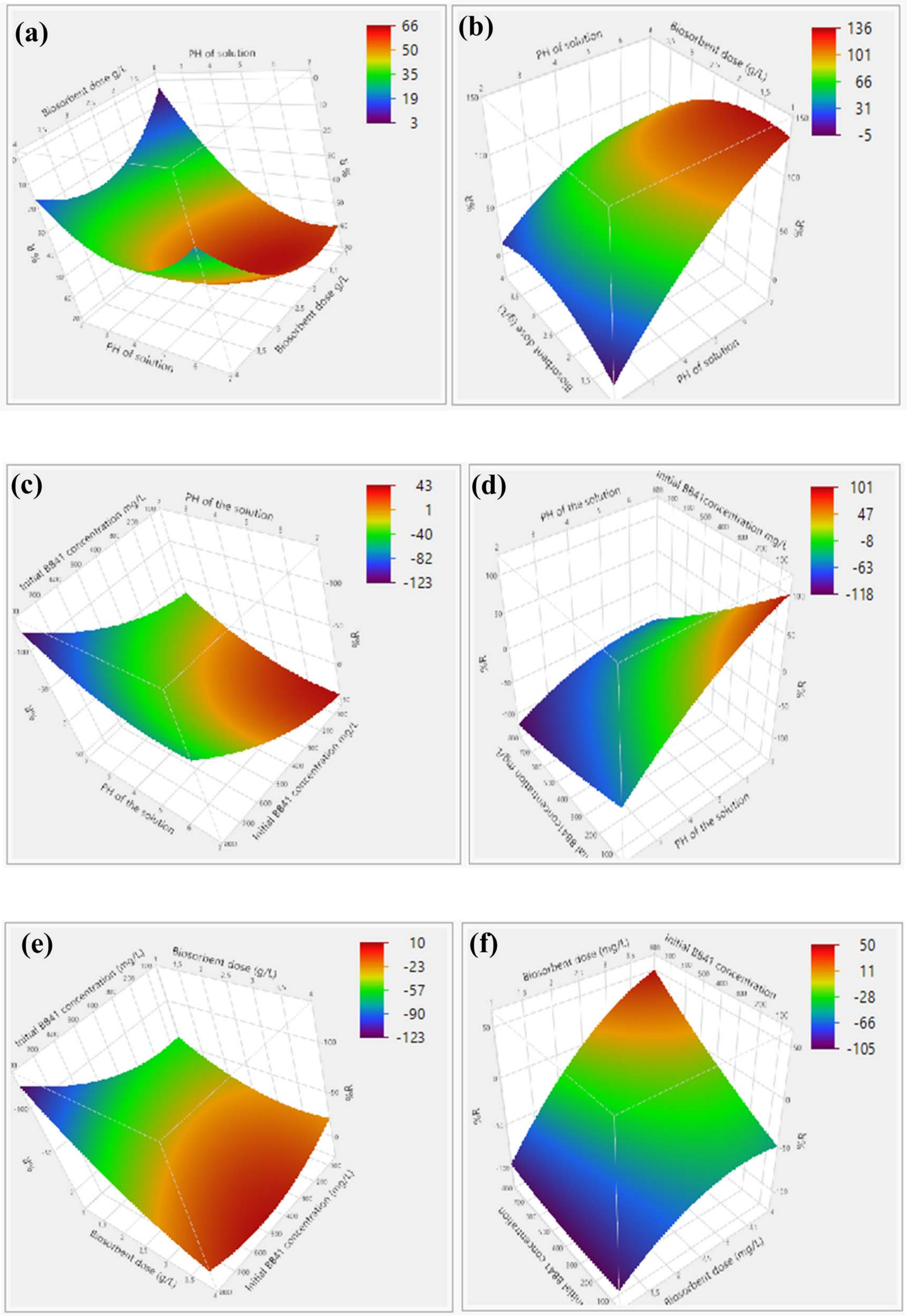

Fig. 8 Response surface plots (3D) of BB41 removal *versus* the effects (pH of solution, biosorbent dose, and initial BB41 concentration), where (a, c, and e) represent untreated biomass, and (b, d, and f) represent treated biomass.

treated and untreated biomass, respectively. The results show the impact of pH levels ranging from 3.01 to 6.99, with an initial BB41 concentration between 200 and 800 mg L^{-1} and a fixed biosorbent dosage of 2.49. The removal efficacy of BB41 was observed to increase significantly with rising pH, reaching optimal adsorption at higher pH values when the initial BB41

Table 8 Optimal BB41 adsorption conditions, predicted removal efficiencies, prediction standard deviations, and 95% confidence intervals for SA and SA-OH

Adsorbent	pH	Biosorbent dose (mg L^{-1})	Initial BB41 concentration (mg L^{-1})	Predicted removal (%)	SD (standard deviation, %)	IC 95
SA	5.31	3	339	76	±2.5	[71;81]
SA-OH	6.99	2	202	97	±2.9	[85;97]

Table 9 Equations and parameters of adsorption isotherms[39]

Isotherm model	Equations	Parameters of adsorption isotherms
Langmuir	$q_e = \dfrac{q_{\max} K_L C_e}{(1 + K_L C_e)}$	$q_{\max}$ (mg g^{-1}): maximum adsorption capacity (mg g^{-1}) K_L: Langmuir constant
Freundlich	$q_e = K_F Ce^{1/n_F}$	n_F: Freundlich constant representing the adsorption intensity K_F (mg$^{(1-n)}$ L^n g^{-1}): Freundlich constant representing the adsorption capacity
Temkin	$q_e = B\ln(A_T C_e)$ $B = \dfrac{RT}{b_T}$	A_T (L mg^{-1}): Temkin constant corresponding to the maximum binding energy b_t (J mol^{-1}): variation in adsorption energy
Sips	$q_e = \dfrac{(q_s K_s {C_e}^{n_s})}{(1 + K_s {C_e}^{n_s})}$	q_s (mg g^{-1}): monolayer adsorption capacity K_s (L mg^{-1}): Sips constant related to adsorption energy n_s: Sips constant
Redlich– Peterson	$q_e = \dfrac{K_{RP} C_e}{(1 + a_R {C_e}^{\beta})}$	K_{RP} (L mg^{-1}): model constant a_R (L mg^{-1}): model constant β: exponent ranging between 0 and 1

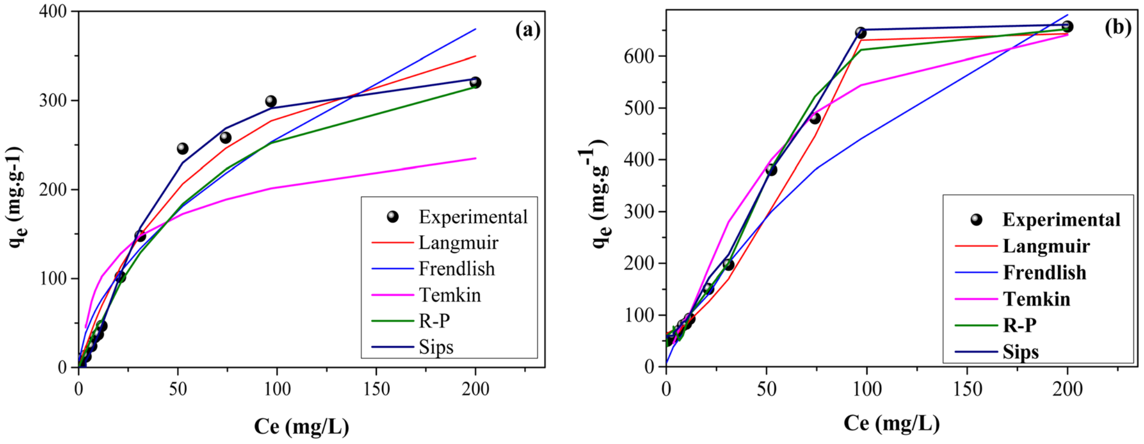

Fig. 9 Representation of the theoretical and experimental adsorption isotherm curves: (a) SA and (b) SA-OH ($m_{a-SA} = 3$ g L^{-1}, $m_{a-SA\text{-}OH}) = 2$ g L^{-1}, pH 5.95, $T = 25$ °C).

concentration was moderate. This phenomenon was attributed to the progressive deprotonation of acidic functional groups (–COOH, –OH) on the biosorbent surface within the studied pH range, which was favorable for biosorption at low BB41 concentrations. Consequently, the electrostatic interaction between the negatively charged biosorbent and the cationic BB41 molecules was strengthened as the surface charge became less positive and more negative. At high BB41 concentrations, the removal efficacy of both untreated and treated biomass declined due to saturation of the available adsorption sites. The surface plot (Fig. 8(e and f)) illustrates the efficacy of BB41 removal by simultaneously varying the biosorbent dosage (1.6–4 g L^{-1}) and the initial BB41 concentration (200–800 mg L^{-1}), while maintaining a constant pH of 4.49.

The predicted removal efficiency for BB41 was estimated to be 76% and 97%, for untreated and treated adsorbent, respectively, under optimal conditions, which included a pH of 5.31 and 6.99, a biosorbent dosage of 3 and 2 g L^{-1}, and an initial BB41 concentration of 339 and 202 mg L^{-1}. The experimental results obtained under these optimized conditions were consistent with the theoretical values. The corresponding predicted standard deviations (2.5% and 2.9%) and 95% confidence intervals (71–81% for SA and 85–97% for SA-OH) are reported in Table 8.

Table 10 Parameters of adsorption isotherm models for BB41 on both adsorbents

Model	Parameters	Untreated biomass	Treated biomass
Langmuir	q_{exp} (mg g^{-1})	320.181	656.456
	q_{max} (mg g^{-1})	314	642.848
	b (L mg^{-1})	0.008	0.13
	R^2	0.94	0.97
Freundlich	K_{F} ((mg g^{-1}) (mg L^{-1})$^{-1/n}$)	7.623	19.443
	n	1.86	1.82
	R^2	0.90	0.91
Temkin	b_{T} (kJ mol^{-1})	0.281	0.371
	B	69.681	92.092
	A_{T} (L g^{-1})	0.134	0.193
	R^2	0.91	0.94
SIPS	q_{s}	335.55	660.55
	K_{s}	0.023	0.029
	n_{s}	2.033	1.44
	R^2	0.996	0.995
Redlich–Peterson	K_{RP}	2.772	5.49
	a_{R}	3.94	1.225
	B	0.709	1.847
	R^2	0.973	0.981

Table 11 Comparison of the maximum adsorption capacities of the two adsorbents with other adsorbents

Adsorbant	Pollutant	Preparation method	Specific surface area (m^2 g^{-1})	q_{m} (mg g^{-1})	Experimental conditions	Reference
SA	BB41	Alkaline hydroxylation	2.62	314	pH = 5.95, $T = 25$ °C $m_{\text{a-SA}} = 3$g L^{-1}	Present work
SA-OH	BB41	—	885.61	642.828	pH = 5.95, $T = 25$ °C $m_{\text{a-SA-OH}} = 2$g L^{-1}	Present work
Zirconium-modified zeolite (Zr(X)-PCH)	BB41	Clay intercalation and pillaring method using metal species, followed by templating and calcination	401	346	pH = [7–9], $T = 25$ °C $m_{\mathrm{Zr}(X)\text{-PCH}} = 8$ g L^{-1}	78
Activated carbon from filamentous algae (AAC)	BB41	Chemical activation with H_3PO_4, followed by carbonization at 650 °C under N_2 flow	—	125	pH = 9, T = room temperature, $m_{\mathrm{AAC}} = 1$ g L^{-1}	79
Immobilized *Yarrowia lipolytica*	BB41	Calcium alginate entrapment method	—	160.25	pH = 9, $T = 25$ °C, $m = 0.25$ g L^{-1}	80
Nitric acid-functionalized rice husk (NT-RH)	Cd	Chemical activation by nitric acid functionalization	148	48.66	pH = 7, $T = 25$ °C, $m_{\text{(NT-RH)}} = 0.9$ g	81

3.7 Biosorption isotherm

To optimize the adsorbent–adsorbate system for BB41 removal, the most appropriate correlations must be established to accurately represent the experimental equilibrium data. The fitting of the experimental adsorption data of BB41 on both adsorbents to the isotherm models was carried out using the non-linear regression methodology. Five of the most commonly applied non-linear models in the literature, namely the two-parameter models (Langmuir, Freundlich, and Temkin) and the three-parameter models (Sips and Redlich–Peterson), were evaluated to describe the adsorption equilibrium isotherms of BB41 on both adsorbents (Table 9). The parameters of these models were obtained through non-linear regression of the adsorption capacity (q_e) as a function of the equilibrium concentration (C_e), as illustrated in Fig. 9. Table 10 presents the calculated parameter values for the different isotherm models. Based on the R^2 values, the isotherm models were ranked according to their degree of fit as follows: Sips > Redlich–Peterson > Langmuir > Temkin > Freundlich. It was reported by Jegan *et al.* that the Sips isotherm model exhibited the highest correlation coefficient ($R^2 = 0.999$) for the adsorption of Basic Blue 41 (BB41) onto biochar derived from groundnut shells, outperforming other models, including Langmuir, Freundlich, and Toth.[75] Therefore, the Sips model is suggested to represent

Table 12 Equations and parameters of adsorption kinetic models[39]

Kinetic models	Equations	Parameters
Pseudo-first order	$q_t = q_e(1 - e^{-k_1 t})$	q_e (mg g^{-1}): equilibrium adsorption capacity k_1 (min^{-1}): pseudo-first-order adsorption rate constant
Pseudo-second order	$q_t = \dfrac{{q_e}^2 k_2 t}{q_e(k_2 t + 1)}$	q_e (mg g^{-1}): equilibrium adsorption capacity k_1 (min^{-1}): pseudo-second-order adsorption rate constant
Intraparticle diffusion	$q_t = k_{int,i}t^{0.5} + I$	k_{int} (mg g^{-1} min$^{-(1/2)}$): intraparticle diffusion constant I (mg g^{-1}): boundary layer thickness

a combination of Langmuir and Freundlich behaviors. At low concentrations, adsorption takes place as a monolayer on a homogeneous surface, similar to Langmuir. At higher concentrations, the process becomes heterogeneous, resembling the Freundlich model, with variable energy sites and possible interactions between adsorbed molecules.[76] It is also noteworthy that, overall, the other models satisfactorily described the adsorption equilibrium, even though the Sips model remained the best fit. The maximum adsorption capacities (q_{max}) estimated from the Langmuir model were 314 mg g^{-1} and 642.848 mg g^{-1} for SA and SA-OH, respectively. The satisfactory agreement of the experimental data with the Redlich–Peterson model indicated its applicability to BB41 adsorption on both adsorbents. This model represents a hybrid adsorption process, encompassing both homogeneous and heterogeneous adsorption.[77] According to the assumptions of the Temkin model, the heat of adsorption decreases linearly with surface coverage, while the binding energy distribution remains uniform. Moreover, the positive value of the constant related to the heat of adsorption (b_T) indicates that the adsorption of BB41 on both adsorbents is of a physical nature.[39]

Based on the fitting data of the Freundlich model (Table 10), the value of the Freundlich constant was greater than one for both adsorbents. This indicates that adsorption is favorable and that the adsorption process is primarily physical. Moreover, the comparison presented in Table 11 clearly shows that the adsorbents developed in this study exhibit a significantly higher adsorption capacity compared to several reported materials, which highlights their potential as effective and competitive sorbents for water remediation.

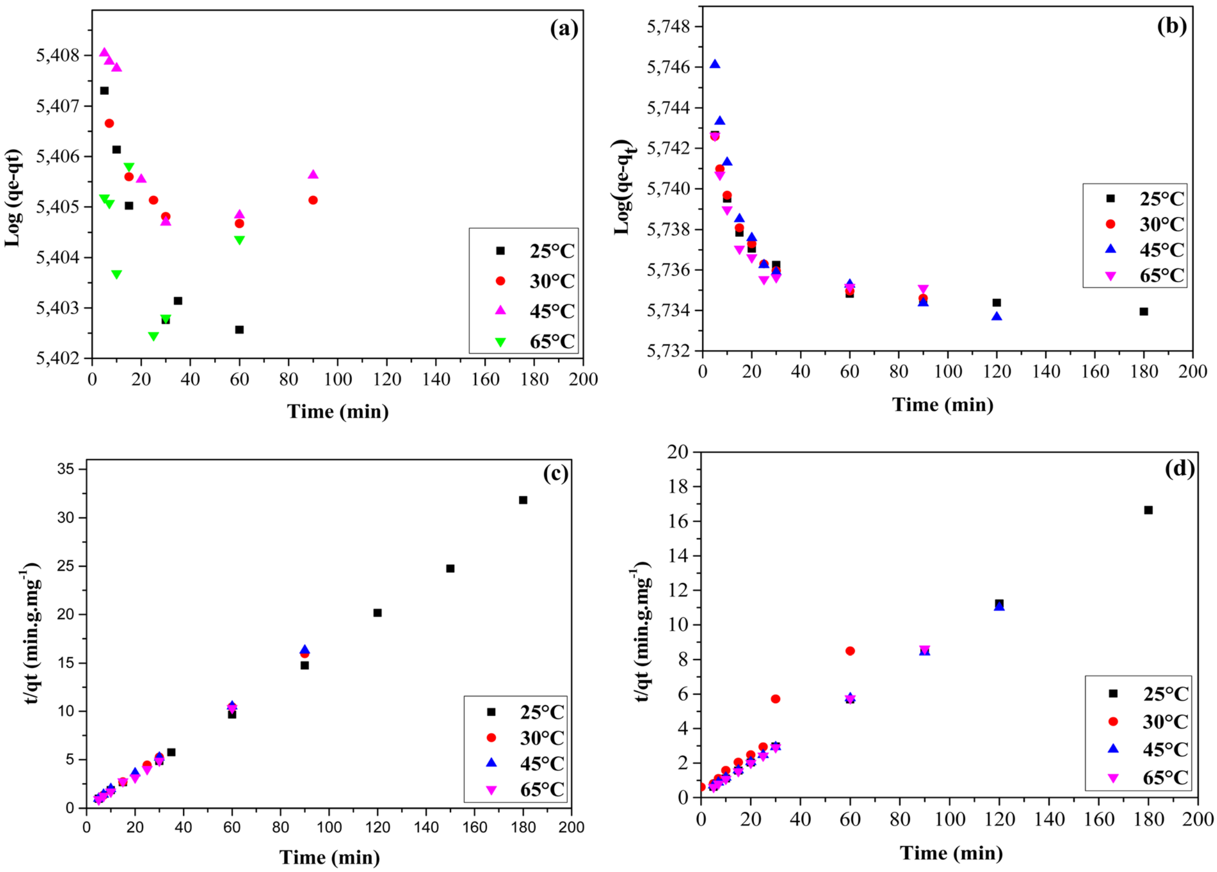

Fig. 10 The pseudo-first-order and pseudo-second-order (a and c) for SA and (b and d) SA-OH.

Table 13 Kinetic parameters of surface reaction models at different temperatures

		Pseudo-first-order			Pseudo-second-order			Experimental
Adsorbents	T (°C)	q_e (mg g^{-1})	k_1 (min^{-1})	R^2	q_e (mg g^{-1})	K_2 (min^{-1})	R^2	q_e (mg g^{-1})
SA-OH	25	5.4	0.47	0.654	10.57	0.8	1	10.3
	30	5.401	0.53	0.401	10.34	0.757	1	10.1
	45	5.413	0.53	0.707	10.76	0.396	0.998	10.85
	65	5.394	0.47	0.738	10.38	0.509	0.999	10.55
SA	25	4.05	0.3	0.550	6.18	0.61	0.99	6.02
	30	2.057	0.53	0.2618	5.81	0.296	0.998	5.35
	45	2.07	0.20	0.318	5.14	0.612	0.993	5.26
	65	3.043	0.13	0.543	5.75	0.66	0.967	5.06

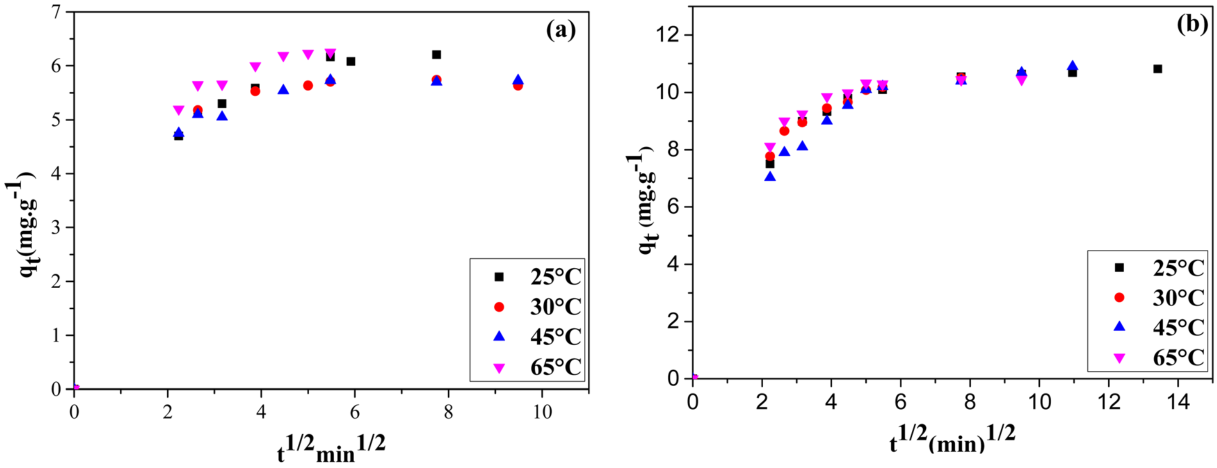

Fig. 11 The intraparticle diffusion model at different temperatures for (a) SA and (b) SA-OH.

3.8 Biosorption kinetics

The kinetic study of BB41 biosorption was performed on both adsorbents, at various initial temperatures, with an initial concentration of 20 mg L^{-1}, using dosages of 3 g L^{-1} for raw biomass and 2 g L^{-1} for treated biomass. This approach provided insights into biosorption modeling and enabled the prediction of the biosorption rate. The pseudo-first-order, pseudo-second-order, and intraparticle diffusion models were applied for the analysis. The equations and parameters of each kinetic model are presented in Table 12. Fig. 10a–d show the kinetic analyses using the pseudo-first-order and pseudo-second-order models, respectively. The model constants are presented in Table 13. The pseudo-second-order model is more suitable for describing the experimental results for both adsorbents, in the temperature range 25–65 mg L^{-1}, as evidenced by high correlation coefficients ($R^2 > 0.99$). This strong agreement indicates that the adsorption rate is mainly governed by the availability of active sites on the adsorbent surface.[82] Furthermore, the calculated equilibrium biosorption capacities closely matched the experimental values. According to the results presented in Table 13, temperature has a notable effect on the rate constant k_2. Specifically, this rate constant increases with temperature, in accordance with the Arrhenius law. The Weber and Morris model was applied to study the diffusivity of Basic Blue 41 (BB41) through the particles of both adsorbents. A linear plot of q_t *versus* $t^{1/2}$ passing through the origin would indicate intraparticle diffusion as the sole rate-limiting step. However, the plots of q_t *versus* $t^{1/2}$ (Fig. 11) exhibited multi-linearity, with correlation coefficients (R^2) between 0.90 and 0.99, and the lines did not pass through the origin, indicating a boundary layer effect.[39] These results suggest that intraparticle diffusion is not the sole rate-limiting factor; the adsorption process may also be influenced by other mechanisms, including

Table 14 Kinetic parameters of the intraparticle diffusion model at different temperatures

	Intraparticle diffusion model			
Adsorbent	T (°C)	K_{id} (mg g^{-1} min$^{0.5}$)	C (mg g^{-1})	R^2
SA	25	0.322	4.398	0.999
	30	0.106	5.116	0.983
	45	0.297	4.144	0.969
	65	0.203	5.261	0.987
SA-OH	25	0.424	7.86	0.928
	30	0.502	7.511	0.978
	45	0.717	7.430	0.946
	65	0.45	7.962	0.906

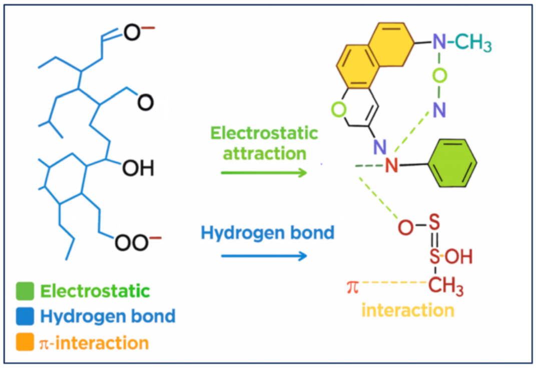

Fig. 12 BB41 adsorption mechanism onto SA-OH.

film diffusion. According to the results shown in Table 14, as the temperature increased from 25 °C to 65 °C, the thickness of the mass transfer boundary layer remained nearly constant.

3.9 Adsorption mechanism of BB41 onto modified lignocellulosic biomass

The process of adsorbing the cationic dye Basic Blue 41 (BB41) onto lignocellulosic biomass modified with H_2O_2 and NaOH involves a variety of physicochemical interactions. By chemically modifying the biomass, reactive oxygen-containing functional groups such as hydroxyl (–OH) and carboxylate ($-COO^-$) were introduced onto its surface. Fig. 12 illustrates three major interactions that facilitate the adsorption mechanism. Initially, electrostatic attraction was observed between the negatively charged carboxylate groups on the biomass and the positively charged quaternary ammonium group (N^+-CH_3) of BB41. This assumption was supported by the observed increase in zeta potential after BB41 adsorption, indicating partial neutralization of surface charges by the dye molecules. In addition, FTIR spectra showed a reduction in the intensity of OH and C=O bands after adsorption, confirming the involvement of these groups in the binding process. Subsequently, hydrogen bonding occurred between the hydroxyl groups of the biomass and the electronegative atoms inside the dye's structure. This interaction is consistent with FTIR changes observed after adsorption, which demonstrated that hydroxyl groups were actively engaged in the binding process. Ultimately, π–π stacking interactions were identified between the aromatic rings of the lignin-rich biomass and those of BB41. A similar mechanism was also reported by other researchers.[83] The synergistic effect of these interactions enhances the dye's binding affinity, resulting in high-performance adsorption efficiency.

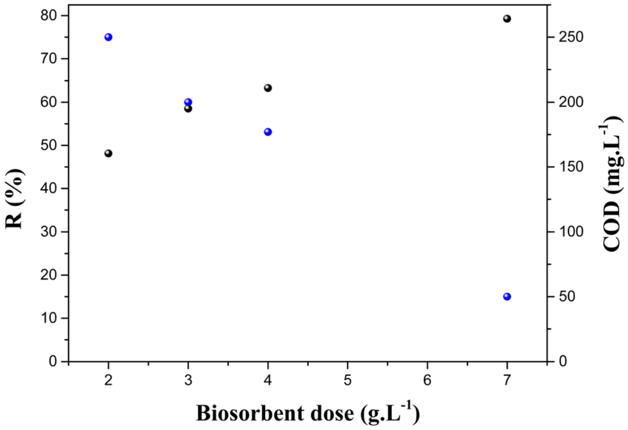

Fig. 13 Evolution of the adsorption efficiency of pollutants on the raw adsorbent and COD as a function of mass (pH 7.72, $t_{eq} = 30$ min, $T = 25$ °C).

3.10 BB1 desorption study

Detailed results on the recyclability and reusability of the adsorbent over multiple adsorption–desorption cycles, using different desorbing agents, are provided in the SI.

3.11 Application to wastewater

Liquid waste was collected from the SEAAL of the Baraki wastewater treatment plant, the primary facility in Algiers. This plant is responsible for treating wastewater from urban areas, as well as industrial and domestic sources from surrounding communities. Based on these properties, biomass treatment can be regarded as an eco-friendly and effective adsorbent for water treatment. To validate the performance of the SA-OH adsorbent and to evaluate whether adsorption was influenced by other pollutants (NO_3^- and Cl^-), SA-OH was applied to treat contaminated wastewater. The physicochemical characteristics of the groundwater are presented in Table 15. Various adsorbent dosages of 2 g L^{-1}, 3 g L^{-1}, 4 g L^{-1}, and 7 g L^{-1} were tested, while other parameters were kept constant (pH 7.7 and $T = 25$ °C). According to the results shown in Fig. 13 and Table 15, the adsorption efficiency increased with increasing adsorbent dosage. Specifically, the efficiency rose from 48.13% to 80%

Table 15 Physicochemical characteristics of wastewater before and after adsorption, and discharge standards

Physico-chemical parameters	Wastewater (before adsorption)	Wastewater (after adsorption)	Standard
pH	7.52	7	6–8
COD (mg L^{-1}) (chemical oxygen demand)	400	50	<125
BOD_5 (mg L^{-1}) (biochemical oxygen demand after 5 days)	250	15	<25
TSS (mg L^{-1}) (total suspended solids)	132	22	<30
Nitrates (mg L^{-1})	45	25	<50
Chlorides (mg L^{-1})	546.87	275	<250

when the mass of the adsorbent was increased from 2 to 7 g L^{-1}. This trend is clearly illustrated by the decrease in chemical oxygen demand (COD) levels and the corresponding increase in removal efficiency. The higher adsorbent dosage provided a greater number of active sites, thereby enhancing the capture and elimination of pollutants. Among the dosages tested, 7 g L^{-1} was identified as the optimum value, as it achieved the highest adsorption efficiency and the greatest reduction in COD levels. With respect to total suspended solids (TSS), a significant reduction was observed, decreasing from 132 mg L^{-1} to 22 mg L^{-1}. Importantly, this value met the discharge standard of 35 mg L^{-1}, confirming the effective removal of suspended solids by the adsorption process. Therefore, SA-OH can be considered a promising adsorbent for wastewater treatment at an industrial scale.

4 Conclusions

This study aimed to valorize a low-cost and readily available industrial waste in Algeria by assessing its potential as a bioadsorbent for the removal of the cationic dye Basic Blue 41 (BB41) from aqueous solutions. Both raw (SA) and chemically modified (SA-OH) forms of the biomass were investigated. The results demonstrated that hydroxylation significantly enhanced the adsorption performance, with SA-OH achieving notably higher removal efficiencies. Process optimization using Response Surface Methodology (RSM) coupled with Central Composite Design (CCD) revealed that pH, adsorbent dosage, and initial dye concentration significantly influenced BB41 removal. The quadratic model provided a good fit for the experimental data, and optimal conditions led to predicted removal efficiencies of 76% for SA and 97% for SA-OH. Equilibrium data were best described by the Langmuir isotherm model, with maximum adsorption capacities of 314 mg g^{-1} for SA and 642.85 mg g^{-1} for SA-OH. Kinetic analysis indicated that the adsorption process followed the pseudo-second-order model, while intraparticle diffusion was not the rate-limiting step. Overall, this work highlights the potential of chemically treated agricultural waste as an efficient and sustainable adsorbent for wastewater treatment applications. These findings provide valuable insights for the development of low-cost materials for environmental remediation. Finally, these data will be valuable for future research on industrial wastewater treatment and the development of adsorbents for wastewater remediation.

Author contributions

Methodology and Investigation: S. B. (Soumia Bakhta), N. B. (Noreddine Boudechiche), and Z. S. (Zahra Sadaoui), formal analysis and investigation: H. H. (Haroun Hafsa), Validation, resources, and supervision: J. V. (Julien Vieillard) and K. S. (Karima Sellami), Writing original draft, review, and editing: S. B., N. B., Z. S., H. H., J. V., K. S.

Conflicts of interest

The authors declare that there are no competing interests or potential conflicts of interest to disclose.

Data availability

All data supporting the findings of this study are included within the article. Additional data can be made available from the corresponding author upon reasonable request.

Supplementary information: additional results on BB41 dye desorption and adsorbent regeneration studies; experimental details, central composite design matrices, ANOVA tables, regression equations, 3D response surface plots, and statistical analyses supporting the optimization and modeling of the desorption process. See DOI: https://doi.org/10.1039/d5ra05466d.

Acknowledgements

This work was funded by the University of Rouen Normandy, INSA Rouen Normandy, the Centre National de la Recherche Scientifique (CNRS), the European Regional Development Fund (ERDF), the Labex SynOrg (ANR-11-LABX-0029), the Carnot Institut I2C, the Graduate School for Research Xl-Chem (ANR-18-EURE-0020 XL CHEM), the EPN agglomeration, and by the Region Normandie.

References

1 R. N. A. Andriambahiny, *et al.*, *Discov. Chem.*, 2025, **2**, 92, DOI: **10.1007/s44371-025-00180-5**.

2 A. Moteallemi, *et al.*, *Environ. Sci. Eur.*, 2025, **37**, 115, DOI: **10.1186/s12302-025-01172-z**.

3 A. P. Periyasamy, *et al.*, Recent Advances in the Remediation of Textile-Dye-Containing Wastewater: Prioritizing Human Health and Sustainable Wastewater Treatment, *Sustainability*, 2024, **15**(16), 5567, DOI: **10.3390/ma15165567**.

4 M. R. I. Rofi and M. R. Rahman, A critical review on environmental pollution caused by the textile industry, *Explora: Environment and Resource*, 2025, **2**(2), 025160032, DOI: **10.36922/EER025160032**.

5 L. A. Castillo-Suárez, *et al.*, *Int. J. Environ. Sci. Technol.*, 2023, **20**, 10553–10590, DOI: **10.1007/s13762-023-04810-2**.

6 D. A. Yaseen and M. Scholz, *Int. J. Environ. Sci. Technol.*, 2019, **16**, 1193–1226, DOI: **10.1007/s13762-018-2130-z**.

7 M. S. Akhtar, *et al.*, Innovative Adsorbents for Pollutant Removal: Exploring the Latest Research and Applications, *Molecules*, 2024, **29**(18), 4317, DOI: **10.3390/molecules29184317**.

8 Y. Wang, *et al.*, *Nanomaterials*, 2019, **9**, 439.

9 G. Crini and E. Lichtfouse, *Environ. Chem. Lett.*, 2019, **17**, 145–155, DOI: **10.1007/s10311-018-0785-9**.

10 A. Kassa, *et al.*, *Desalination Water Treat.*, 2025, **323**, 101362, DOI: **10.1016/j.dwt.2025.101362**.

11 K. S. Bharathi and S. T. Ramesh, *Appl. Water Sci.*, 2013, **3**, 773–790, DOI: **10.1007/s13201-013-0117-y**.

12 E. K. Tsoutsa, *et al.*, *Water, Air, Soil Pollut.*, 2024, **235**, 178, DOI: **10.1007/s11270-024-06979-9**.

13 K. Ali, *et al.*, *Desalination Water Treat.*, 2023, **302**, 231–252, DOI: **10.5004/dwt.2023.29725**.

14 H. S. Rangappa, *et al.*, *Environ. Pollut.*, 2024, **343**, 123140, DOI: 10.1016/j.envpol.2023.123140.
15 M. Ahmaruzzaman, *Adv. Colloid Interface Sci.*, 2011, **166**, 36–59, DOI: 10.1016/j.cis.2011.04.005.
16 T. Wang, *et al.*, *Sep. Purif. Technol.*, 2022, **302**, 122116, DOI: 10.1016/j.seppur.2022.122116.
17 H. Yang, *et al.*, *Energy*, 2025, **323**, 135806, DOI: 10.1016/j.energy.2025.135806.
18 S. Pu, *et al.*, *PLoS One*, 2018, **13**, e0190236, DOI: 10.1371/journal.pone.0190236.
19 S. Tamjidi, *et al.*, *Phys. Chem. Res.*, 2024, **12**, 361–382, DOI: 10.22036/pcr.2023.396003.2332.
20 E. A. B. d. Silva, *et al.*, *Chem. Eng. Res. Des.*, 2009, **87**, 1276–1292, DOI: 10.1016/j.cherd.2009.05.008.
21 E. S. Tarleton and R. J. Wakeman, *Solid/Liquid Separation: Equipment Selection and Process Design*, Elsevier, 2006.
22 J. Ji, *et al.*, *J. Hazard. Mater.*, 2022, **430**, 128375, DOI: 10.1016/j.jhazmat.2022.128375.
23 S. M. Abegunde, *et al.*, *Resour. Environ. Sustain.*, 2020, **1**, 100001, DOI: 10.1016/j.resenv.2020.100001.
24 G. Liu, *et al.*, *Carbon Res.*, 2022, **1**, 24, DOI: 10.1007/s44246-022-00025-1.
25 B. E. Tokula, *et al.*, *J. Clean. Prod.*, 2023, **388**, 135819, DOI: 10.1016/j.jclepro.2022.135819.
26 S. E. Manahan, *Fundamentals of Environmental Chemistry*, third edition, CRC Press, 2008.
27 B. K. Pradhan and N. K. Sandle, *Carbon*, 1999, **37**, 1323–1332, DOI: 10.1016/S0008-6223(98)00328-5.
28 J. Kim, *et al.*, Enhancing Response Surface Methodology through Coefficient Clipping Based on Prior Knowledge, *Processes*, 2023, **11**(12), 3392, DOI: 10.3390/pr11123392.
29 R. H. Myers, *et al.*, *Response Surface Methodology: Process and Product Optimization Using Designed Experiments*, fourth edition, Wiley, 2016.
30 A. T. Nair, *et al.*, *Water Sci. Technol.*, 2014, **69**, 464–478, DOI: 10.2166/wst.2013.733.
31 A. Asfaram, *et al.*, *J. Mol. Liq.*, 2016, **214**, 249–258, DOI: 10.1016/j.molliq.2015.12.075.
32 A. Czyrski and H. Jarzębski, *Processes*, 2020, **8**, 473.
33 R. Ghelich, *et al.*, *Composites, Part B*, 2019, **166**, 527–541, DOI: 10.1016/j.compositesb.2019.01.094.
34 S. Bhattacharya, *Central Composite Design for Response Surface Methodology and its Application in Pharmacy*, IntechOpen, 2021.
35 S. Afshar, *et al.*, *Monatsh. Chem.*, 2015, **146**, 1949–1957, DOI: 10.1007/s00706-015-1533-5.
36 S. Humberg, *et al.*, *Psychol. Methods*, 2020, **27**, 622–649, DOI: 10.1037/met0000352.
37 D. Podstawczyk, *et al.*, *Ecol. Eng.*, 2015, **83**, 364–379, DOI: 10.1016/j.ecoleng.2015.07.004.
38 H. Hafsa, *et al.*, *Arabian J. Sci. Eng.*, 2025, DOI: 10.1007/s13369-025-10394-5.
39 S. Bakhta, *et al.*, *RSC Adv.*, 2022, **12**, 2332–2348, DOI: 10.1039/D1RA08209D.
40 L. Yahia Cherif, *et al.*, *Ind. Eng. Chem. Res.*, 2014, **53**, 3813–3819, DOI: 10.1021/ie403970m.
41 S. Sadri Moghaddam, *et al.*, *J. Hazard. Mater.*, 2010, **175**, 651–657, DOI: 10.1016/j.jhazmat.2009.10.058.
42 P. Pocasap, *et al.*, FTIR Microspectroscopy for the Assessment of Mycoplasmas in HepG2 Cell Culture, *Appl. Sci.*, 2020, **10**(11), 3766, DOI: 10.3390/app10113766.
43 A. Emandi, *et al.*, *Cellul. Chem. Technol.*, 2011, **45**, 579–584.
44 T. Hong, *et al.*, *Food Chem.:X*, 2021, **12**, 100168, DOI: 10.1016/j.fochx.2021.100168.
45 A.-M. Olsson and L. Salmén, *Carbohydr. Res.*, 2004, **339**, 813–818, DOI: 10.1016/j.carres.2004.01.005.
46 U. P. Agarwal, *et al.*, *J. Wood Chem. Technol.*, 2011, **31**, 324–344, DOI: 10.1080/02773813.2011.562338.
47 Y. Nashchekina, *et al.*, Collagen Scaffolds Treated by Hydrogen Peroxide for Cell Cultivation, *Polymers*, 2021, **13**(23), 4134, DOI: 10.3390/polym13234134.
48 J. Popović, *et al.*, Research Article or Brief Communication, vol. **17**, 2022.
49 S. F. Sim, *et al.*, *Bioresources*, 2014, **9**, 952–968.
50 X. Hu, *et al.*, *Colloids Surf., A*, 2022, **643**, 128782, DOI: 10.1016/j.colsurfa.2022.128782.
51 E. A. Moawed, *et al.*, *Int. J. Environ. Sci. Technol.*, 2019, **16**, 8495–8504, DOI: 10.1007/s13762-019-02343-1.
52 X. Fu, *et al.*, *Sep. Purif. Technol.*, 2025, **360**, 131196, DOI: 10.1016/j.seppur.2024.131196.
53 X. Meng, *et al.*, *Bioresour. Technol.*, 2013, **144**, 467–476, DOI: 10.1016/j.biortech.2013.06.091.
54 C. A. Rezende, *et al.*, *Biotechnol. Biofuels*, 2011, **4**, 54, DOI: 10.1186/1754-6834-4-54.
55 M. Li, *et al.*, *Biotechnol. Biofuels*, 2012, **5**, 38, DOI: 10.1186/1754-6834-5-38.
56 J. Mao, *et al.*, *Biomass Bioenergy*, 2024, **185**, 107233, DOI: 10.1016/j.biombioe.2024.107233.
57 Y. Zhan, *et al.*, *Ind. Crops Prod.*, 2024, **214**, 118533, DOI: 10.1016/j.indcrop.2024.118533.
58 H. Zhang and J. Wu, *Fermentation*, 2023, **9**, 871.
59 H. Zhang, *et al.*, *Biotechnol. Biofuels*, 2019, **12**, 107, DOI: 10.1186/s13068-019-1454-3.
60 A. K. Tareen, *et al.*, *3 Biotech*, 2020, **10**, 179, DOI: 10.1007/s13205-020-02169-6.
61 J. Shin, *et al.*, *J. Hazard. Mater.*, 2022, **435**, 129081, DOI: 10.1016/j.jhazmat.2022.129081.
62 D. Q. Lin, *et al.*, *Biotechnol. Bioeng.*, 2006, **95**, 185–191, DOI: 10.1002/bit.21011.
63 J. N. Miller, *Analyst*, 1991, **116**, 3–14, DOI: 10.1039/AN9911600003.
64 J. Sajedifar, *et al.*, *Heliyon*, 2024, **10**, e38087, DOI: 10.1016/j.heliyon.2024.e38087.
65 L. C. Almeida, *et al.*, *Appl. Catal., B*, 2011, **103**, 21–30, DOI: 10.1016/j.apcatb.2011.01.003.
66 E. L. Soo, *et al.*, *Process Biochem.*, 2004, **39**, 1511–1518, DOI: 10.1016/S0032-9592(03)00279-6.
67 S. Bzovsky, *et al.*, *Eye*, 2022, **36**, 1715–1717, DOI: 10.1038/s41433-022-01949-z.
68 N. Sivarajasekar and R. Baskar, *J. Ind. Eng. Chem.*, 2014, **20**, 2699–2709, DOI: 10.1016/j.jiec.2013.10.058.
69 K. Anupam, *et al.*, *Desalination Water Treat.*, 2016, **57**, 3632–3641, DOI: 10.1080/19443994.2014.987172.

70 K. V. Kumar and K. Porkodi, *Chem. Eng. J.*, 2009, **148**, 20–25, DOI: 10.1016/j.cej.2008.07.026.

71 S. Dutta, *et al.*, *Desalination*, 2011, **275**, 26–36, DOI: 10.1016/j.desal.2011.02.057.

72 N. K. Mondal, *et al.*, *Appl. Water Sci.*, 2019, **9**, 116, DOI: 10.1007/s13201-019-0997-6.

73 S. D. Salman, *et al.*, *Desalination Water Treat.*, 2024, **317**, 100246, DOI: 10.1016/j.dwt.2024.100246.

74 N. Sivarajasekar, *et al.*, *Appl. Water Sci.*, 2017, **7**, 1987–1995, DOI: 10.1007/s13201-016-0379-2.

75 J. Jegan, *et al.*, *Appl. Ecol. Environ. Res.*, 2020, **18**, 1925–1939, DOI: 10.15666/aeer/1801_19251939.

76 K. Y. Foo and B. H. Hameed, *Chem. Eng. J.*, 2010, **156**, 2–10, DOI: 10.1016/j.cej.2009.09.013.

77 L. Nouri, *et al.*, *Int. J. Biol. Macromol.*, 2020, **151**, 66–84, DOI: 10.1016/j.ijbiomac.2020.02.159.

78 S. A. Popoola, *et al.,* Enhancement Properties of Zr Modified Porous Clay Heterostructures for Adsorption of Basic-Blue 41 Dye: Equilibrium, Regeneration, and Single Batch Design Adsorber, *Materials*, 2022, **15**(16), 5567, DOI: 10.3390/ma15165567.

79 S. Afshin, *et al.*, *Data Brief*, 2018, **21**, 1008–1013, DOI: 10.1016/j.dib.2018.10.023.

80 A. H. Hassan Ibrahim, *et al.*, *World J. Microbiol. Biotechnol.*, 2024, **40**, 140, DOI: 10.1007/s11274-024-03949-5.

81 M. Hussain, *et al.*, *Inorg. Chem. Commun.*, 2024, **160**, 112010, DOI: 10.1016/j.inoche.2023.112010.

82 Y. S. Ho and G. McKay, *Process Biochem.*, 1999, **34**, 451–465, DOI: 10.1016/S0032-9592(98)00112-5.

83 A. Hamadi, *et al.*, *J. Food Sci. Technol.*, 2021, **58**, 1081–1092, DOI: 10.1007/s13197-020-04622-z.